Energy Materials

Supplementary Materials

Hierarchically porous two-dimensional Fe/N-codoped carbon nanoleaves for enhanced mass transfer and electrocatalytic oxygen reduction reaction

Limin Song#, Yining Liu#, Jing-Jing Wang, Ruotong Wu, Jing-Shuang Dang*, Hang Zhang*, Wei Zhang, Rui Cao, Haoquan Zheng*

Key Laboratory of Applied Surface and Colloid Chemistry, Ministry of Education, School of Chemistry and Chemical Engineering, Shaanxi Normal University, Xi'an 710119, Shaanxi, China.

#Authors contributed equally.

***Correspondence to:** Prof. Haoquan Zheng, Assoc. Prof. Hang Zhang, and Assoc. Prof. Jing-Shuang Dang, Key Laboratory of Applied Surface and Colloid Chemistry, Ministry of Education, School of Chemistry and Chemical Engineering, Shaanxi Normal University, No. 620, West Chang'an Avenue, Chang'an District, Xi'an 710119, Shaanxi, China. E-mail: zhenghaoquan@snnu.edu.cn; zhangteacher@snnu.edu.cn; dangjs@snnu.edu.cn

1. Materials characterization

The scanning electron microscopy (SEM) images were acquired using a Hitachi SU8020 field-emission electron microscope. Transmission electron microscopy (TEM) characterization was performed on a JEOL JEM-7900F system operated at 200 kV, coupled with energy-dispersive X-ray spectroscopy (EDS) for elemental mapping of C, N, and Fe distributions in the catalyst. Aberration-corrected high-angle annular dark-field scanning transmission electron microscopy (AC HAADF-STEM) imaging was conducted on a Themis G2 300 microscope at 300 kV accelerating voltage. Crystalline structure analysis was carried out using a Bruker D8 Advance X-ray diffractometer with Cu Kα radiation ($\lambda = 1.5418$ Å) for powder X-ray diffraction (PXRD) pattern collection. Raman spectroscopy measurements were performed on a HORIBA LabRAM Odyssey system equipped with a 532 nm excitation laser. X-ray photoelectron spectroscopy (XPS) data were recorded using a Kratos AXIS ULTRA spectrometer. N_2 adsorption-desorption isotherms were measured using a Micromeritics ASAP 2460 analyzer. The Brunauer-Emmett-Teller (BET) method was employed to calculate specific surface areas, while pore size distributions were derived from adsorption branches using the Barrett-Joyner-Halenda (BJH) model. Fe K-edge X-ray absorption spectroscopy (XAS) data were collected using an easyXAFS300+ spectrometer.

2. Electrochemical measurements

All electrochemical measurements were performed using three-electrode system on a CHI 760E at 25 ± 1°C, with 0.1 M KOH as the electrolyte. A graphite rod served as the counter electrode, and an Ag/AgCl electrode was used as the reference electrode. The working electrode consisted of either a glassy carbon rotating disk electrode (RDE, 5 mm, 0.196 cm^2) or a rotating ring-disk electrode (RRDE, 5.61 mm, 0.247 cm^2).

Catalyst ink was prepared by homogenously dispersing 2 mg catalyst in a mixture of 333 μL H_2O, 166 μL isopropanol, and 10 μL 5 wt% Nafion solution through ultrasonication. The ink was deposited onto the electrode surface via two sequential 10 μL aliquots using a micropipette, followed by air-drying to achieve a uniform catalyst loading of 0.4 mg cm^{-2} (±0.02 mg cm^{-2}).

Cyclic voltammetry (CV) scans were conducted between 0.2 and 1.4 V vs. RHE at 50 mV s^{-1} under Ar/O_2-saturated conditions. Linear sweep voltammetry (LSV) measurements were performed in O_2-saturated electrolyte with 100% iR compensation, employing a scan rate of 5 mV s^{-1} and rotation speeds ranging from 400 to 2025 rpm. All potentials were converted to the reversible hydrogen electrode (RHE) scale using the established calibration equation: $E_{RHE} = E_{Ag/AgCl} + 0.059\ pH + 0.197$.

The electron transfer number (n) was determined by RDE measurements by Koutecký-Levich (K-L) equation:

$$\frac{1}{J} = \frac{1}{J_K} + \frac{1}{J_L} = \frac{1}{J_K} + \frac{1}{B\omega^{\frac{1}{2}}}$$

$$B = 0.62nFC_0D_0^{\frac{2}{3}}V^{-\frac{1}{6}}$$

here, j represents the measured current density, j_L denotes the diffusion–limited current density, and j_K corresponds to the kinetic current density. The parameter ω indicates the angular velocity of the rotating disk electrode. n is the number of transferred electrons, F is the Faraday constant (96485 C mol^{-1}), D_0 is the oxygen diffusion coefficient (1.93×10^{-5} cm^2 s^{-1}), C_0 is the bulk oxygen concentration (1.2×10^{-6} mol cm^{-3}), and V is the kinematic viscosity of the electrolyte (0.01 cm^2 s^{-1}).

For RRDE system, the electron transfer number n and hydrogen peroxide yield (H_2O_2 %) can be calculated through RRDE measurements using the following equations:

$$n = \frac{4I_d}{I_d + \frac{I_r}{n}}$$

$$H_2O_2 yield\ (\%) = \frac{2I_r/N}{I_d + I_r/N} \times 100\%$$

where I_d is the disk current, I_r is the ring current, and N is the current collection efficiency of the platinum (Pt) ring, which is determined to be 0.37 under the given conditions.

The electrochemically active surface area (ECSA) calculated based on the double-layer capacitance (C_{dl}), which was obtained through a series of cyclic voltammetry (CV) within the non-Faradaic potential range of 0.99-1.09 V (vs. RHE) at scan rates ranging from 10 to 100 mV s^{-1}. The ECSA was further calculated by the following equation:

$$ECSA(m^2\ \mathrm{g}^{-1}) = \frac{C_{dl}}{C_s \times L}$$

where C_s is the specific capacitance of the electric double layer (0.04 mF cm^{-2}) and L is the catalyst loading.

3. Zn-air battery measurements

All electrochemical performance tests of zn-air batteries (ZABs) were conducted on the CHI 660E electrochemical workstation. The catalyst ink was prepared by dispersing 2.5 mg of the catalyst and 2.5 mg of Ir/C in a mixture of 960 μL ethanol and 40 μL Nafion solution (5 wt%), followed by ultrasonication for several hours to obtain a homogeneous catalyst suspension. For the Pt/C + Ir/C catalyst ink, a similar preparation method was employed. The anode of the ZABs was a circular zinc plate with a thickness of 0.25 mm and a diameter of 1.5 cm. The surface oxide layer was removed by polishing with sandpaper prior to use. The air cathode was fabricated by hot-pressing carbon cloth (CC, 1.5 × 1.5 cm^2) with a gas diffusion layer (GDL, 1.8 × 1.8 cm^2) at 80O °C for 90 s. Subsequently, 450 μL of the catalyst ink was uniformly drop-cast onto the center of the CC/GDL substrate and dried naturally. The actual electrochemical active area of the battery was approximately 0.785 cm^2, with a catalyst loading of 2 mg cm^{-2}. The electrolyte for the ZABs consisted of a 6 M KOH solution with 0.2 M $Zn(OAc)_2{\cdot}2H_2O$. The discharge profiles and specific capacity were measured at a constant current density of 20 mA cm^{-2}. The cycling performance was evaluated at a current density of 5 mA cm^{-2}, with each cycle consisting of 10 minutes of charging followed by 10 minutes of discharging (total cycle time: 20 minutes). The polarization curves were obtained by linear sweep voltammetry (LSV) at a scan rate of 10 mV s^{-1}. The rate performance of the battery was evaluated by galvanostatic discharge tests. The current density was set successively as 1, 2, 5, 10, 20 mA cm^{-2} and then restored to 1 mA cm^{-2}, with each current density lasting for 30 minutes.

In-situ electrochemical impedance spectroscopy (*In-situ* EIS) was performed on the Meso/Micro-FeNC electrode under operating conditions of a ZAB. A three-electrode system was employed for the EIS measurements, with the frequency range set from 10^5 to 10^{-1} Hz and an amplitude of 10 mV. The ZAB was operated at a charge-discharge current density of 1 mA cm^{-2}, and the sampling cycles consisted of a 30-minute charging process followed by a 30-minute discharging process.

4. Distribution of relaxation time analysis

The distribution of relaxation times (DRT) was calculated using "DRTtools", a software package developed by Francesco Ciucci's team[1]. The Gaussian function was selected as the discretization method. The fitting procedure excluded inductive effects and adopted the following DRT model:

$$Z_{DRT} = R_{\infty} + \int_{-\infty}^{\infty} \frac{\gamma(ln\tau)}{1 + i2\pi f\tau} dln\tau$$

In related calculations, Z_{DRT} is the impedance obtained from the DRT model. $\gamma(ln\tau)$ is the DRT function. τ, f, and R_{∞} are the time scale, frequency, ohmic and impedance, respectively. The regularization derivative is set to 1st-order with a parameter value of 10^{-3}. The shape control is set to be the “FWHM coefficient” with a magnitude of 0.5. The DRT is calculated by the “Bayesian run” method.

5. Computational Methods

To explore how substrate curvature influences both the reaction pathway and catalytic performance of the oxygen reduction reaction (ORR), two representative Fe–N–C models were developed: one based on a flat 6×6 graphene sheet and the other incorporating a negatively curved geometry constructed from hydrogen-terminated semi-cylindrical segments of a zigzag (12,0) carbon nanotube. To preserve the intrinsic curvature of the original nanotube structure, constrained geometry optimizations were employed. Initially, only the terminal hydrogen atoms were allowed to relax. In the subsequent step, the FeN_4 moiety, along with the adjacent ten carbon atoms surrounding the active site and the hydrogen atoms, were kept fixed, while all remaining carbon atoms in the framework and the adsorbed species were fully relaxed. This procedure ensured accurate determination of the intermediate conformations while maintaining the predefined curvature of the substrate.

Spin-polarized calculations were carried out within the framework of density functional theory (DFT), as implemented in the Vienna Ab Initio Simulation Package (VASP)[2], using projector augmented wave (PAW) pseudopotentials[3-4]. The exchange–correlation energy was described using the Perdew–Burke–Ernzerhof (PBE) functional under the generalized gradient approximation (GGA) [5]. A kinetic energy cutoff of 500 eV was applied, with electronic and ionic convergence criteria of 1×10^{-5} eV and 0.02 eV/Å, respectively. Brillouin zone sampling was performed using Gamma-centered k-point meshes of 1×1×2 for the curved model and 2×2×1 for the planar counterpart[6]. To mimic aqueous solvation, an implicit solvation model based on the conductor-like screening model (COSMO) was employed, incorporating a dielectric constant of 78.4 (corresponding to water) via the Poisson–Boltzmann formalism[7].

The oxygen reduction reaction (ORR) pathways were systematically examined using the computational hydrogen electrode (CHE) approach developed by Nørskov and colleagues.[8] Under alkaline conditions (pH = 13), where water (H_2O) acts as the proton source rather than hydronium ions (H_3O^+), the ORR mechanism can be represented by the following sequence of elementary steps:

Step 1: $* + O_2(g) + H_2O(l) + e^- \rightarrow *OOH + OH^-$

Step 2: $*OOH + e^- \rightarrow *O + OH^-$

Step 3: $*O + H_2O(l) + e^- \rightarrow *OH + OH^-$

Step 4: $*OH + e^- \rightarrow * + OH^-$

where * represents the catalyst surface and *OOH, *O and *OH species are oxygenated intermediates.

The reaction free energy of each step can be calculated by:

$$\Delta G = \Delta E + \Delta ZPE - T\Delta S - neU + \mathrm{k_B} T \ln 10 \cdot \mathrm{pH}$$

where ΔE denotes the energy change from reactants to products, ΔZPE represents zero-point energy correction with the temperature of 298.15 K, ΔS indicates the adsorption state and free state entropy correction. U is the applied electrode potential, and n is the number of electron transfer. The last term $k_B T\mathrm{In}10\cdot\mathrm{pH}$ is a correction to the Gibbs free energy of the OH^- anion at a pH value, k_B is the Boltzmann constant, and T is the temperature. Here, we set pH = 13 and $T = 298$ K, respectively. As an important indicator for evaluating the activity of the oxygen reduction reaction, the overpotential (η) is calculated as:

$$\eta = U_0 + \max(\Delta G_1, \Delta G_2, \Delta G_3, \Delta G_4)$$

$$\eta = U_0 + \max\,(\Delta G_1, \Delta G_2, \Delta G_3, \Delta G_4)$$

where ΔG_{max} is the maximum Gibbs free energy change among four elementary steps and $U_0 = 0.46$ V is the equilibrium potential for pH = 13 at T = 298 K.

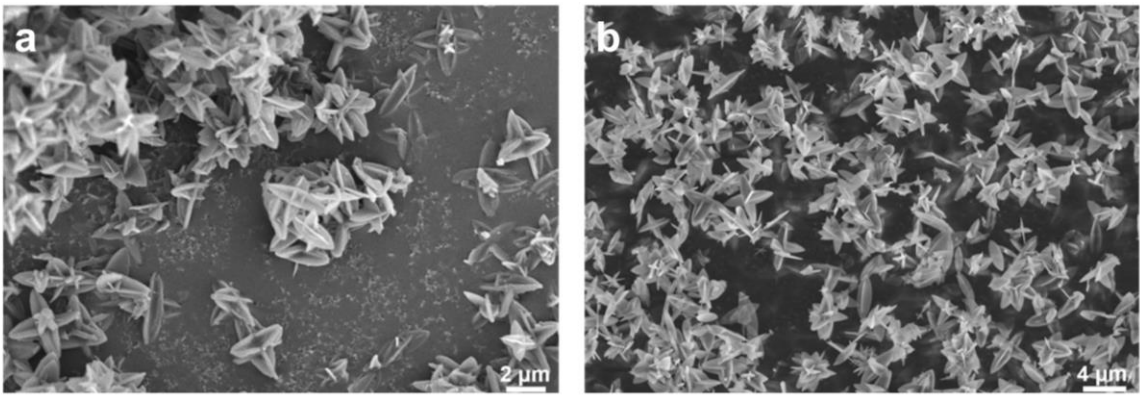

Figure S1. The SEM image of ZIF-L-Fe (a) and Fe-NC (b).

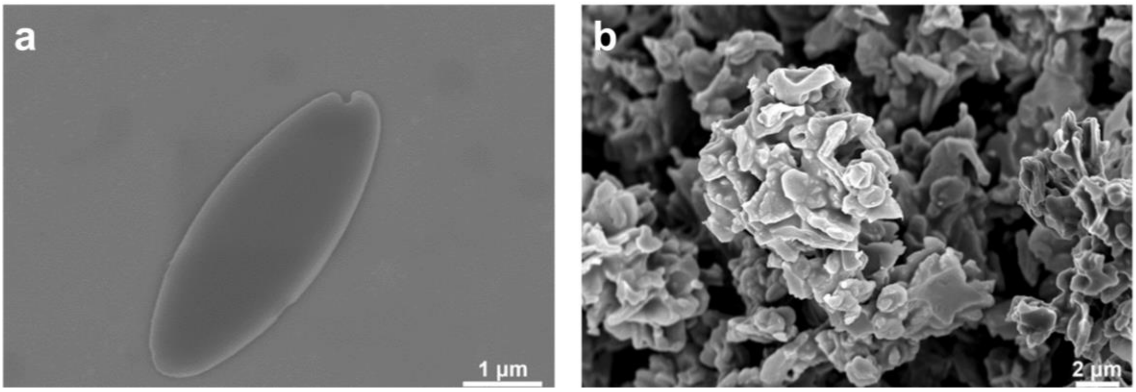

Figure S2. The SEM image of ZIF-L (a) and NC (b).

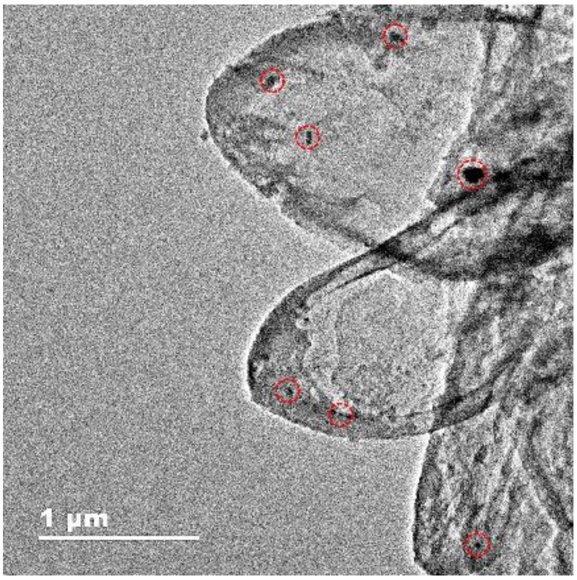

Figure S3. The TEM image of Fe-NC.

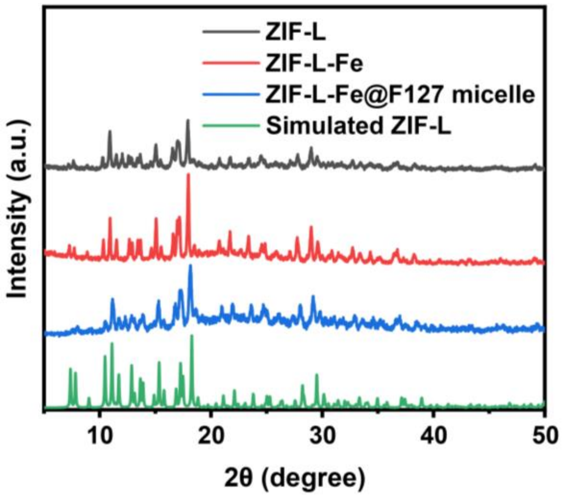

Figure S4. Powder XRD patterns of ZIF-L, ZIF-L-Fe, ZIF-L-Fe@F127 micelle Meso/Micro-FeNC, and simulated ZIF-L.

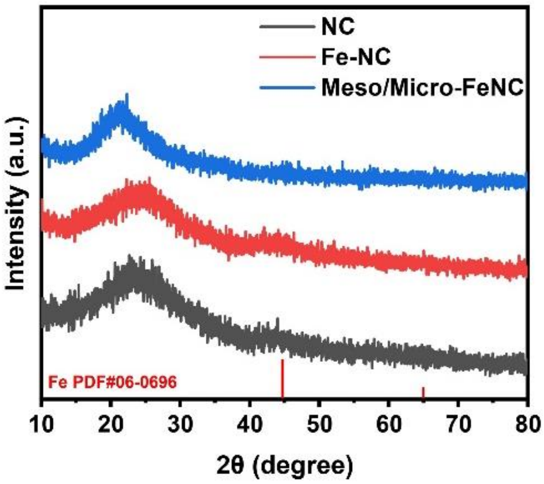

Figure S5. Powder XRD patterns of NC, Fe-NC, and Meso/Micro-FeNC.

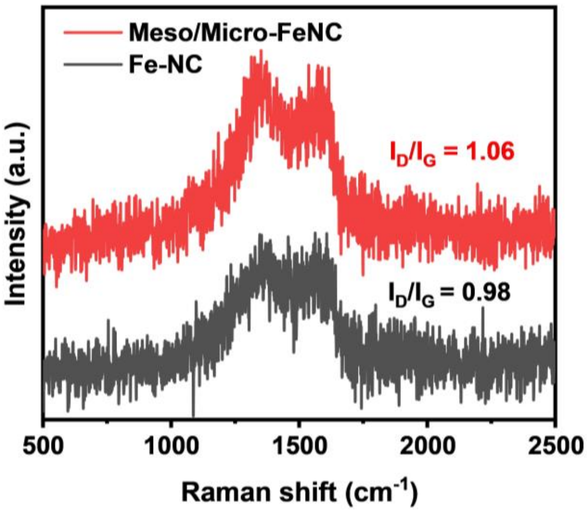

Figure S6. The Raman spectrum of Meso/Micro-FeNC and Fe-NC.

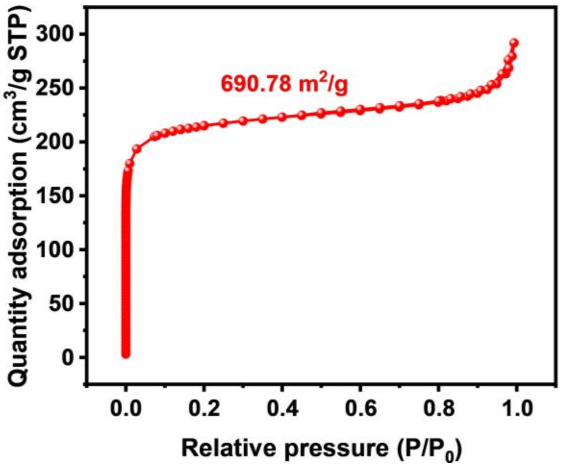

Figure S7. N_2 adsorption/desorption isotherm of Fe-NC.

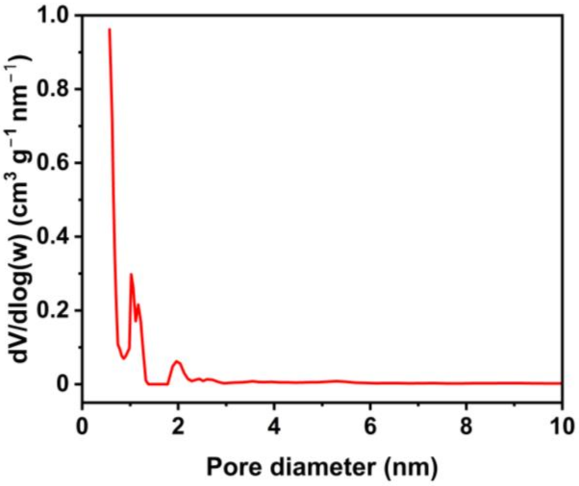

Figure S8. Pore size distribution of Fe-NC based on N_2 adsorption/desorption isotherm.

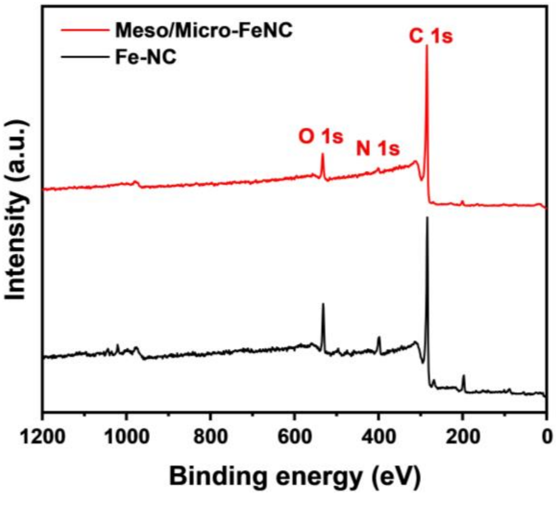

Figure S9. The XPS survey spectrum of Meso/Micro-FeNC and Fe-NC.

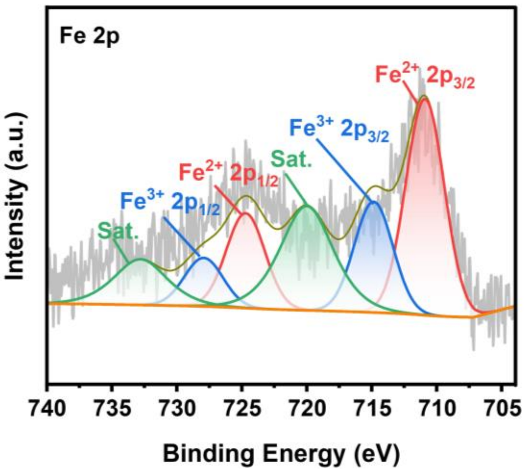

Figure S10. Fe 2p high resolution spectrum of Meso/Micro-FeNC.

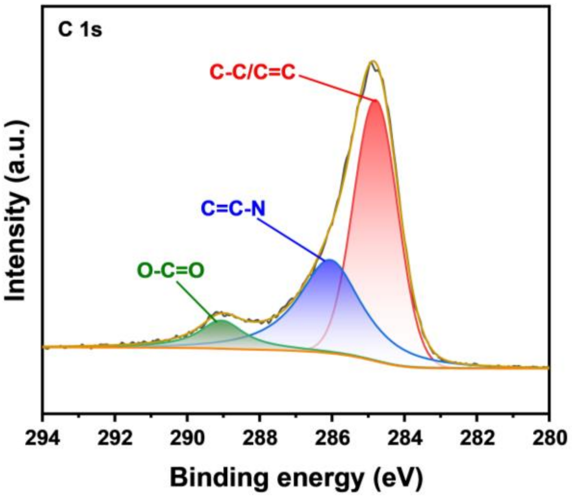

Figure S11. C 1s high resolution spectrum of Fe-NC.

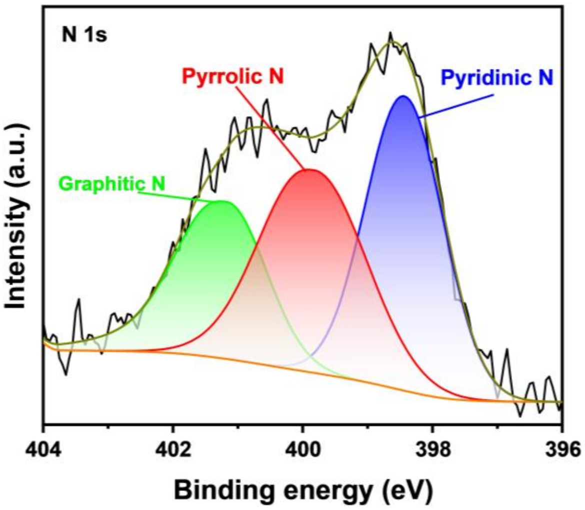

Figure S12. N 1s high resolution spectrum of Fe-NC.

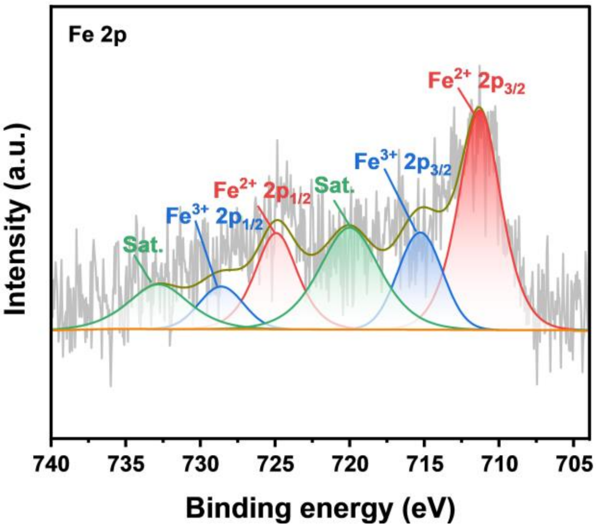

Figure S13. Fe 2p high resolution spectrum of Fe-NC.

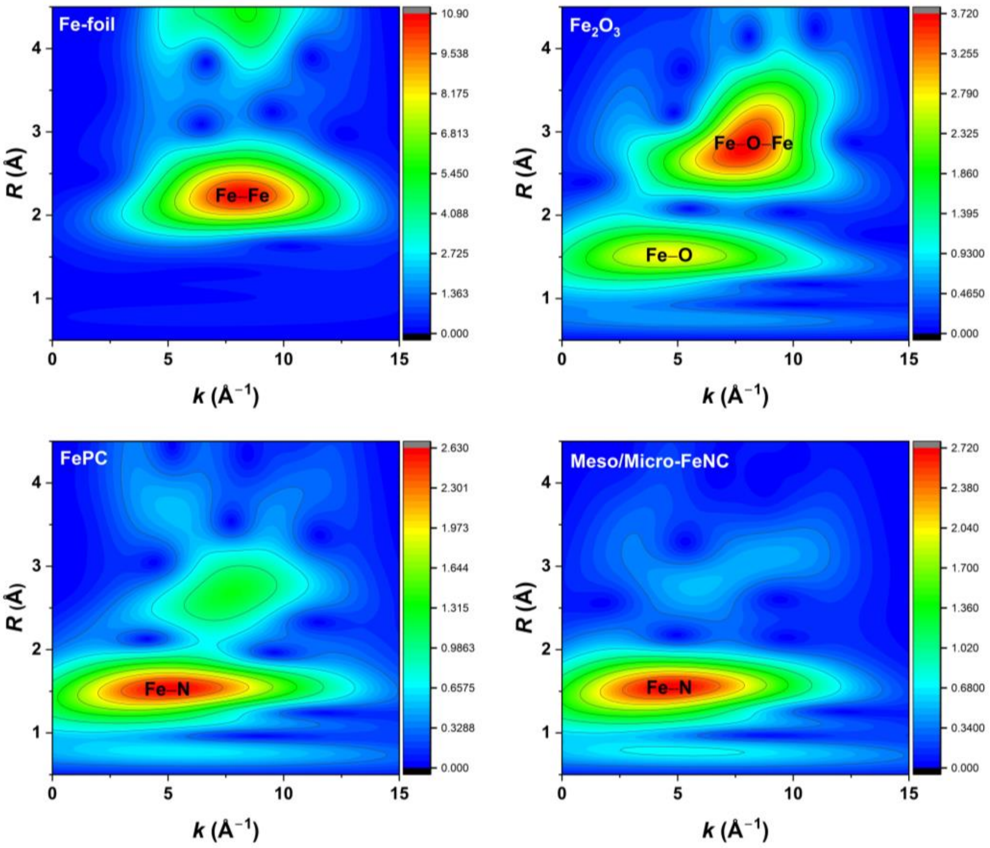

Figure S14. WT plot of Meso/Micro-FeNC and reference samples.

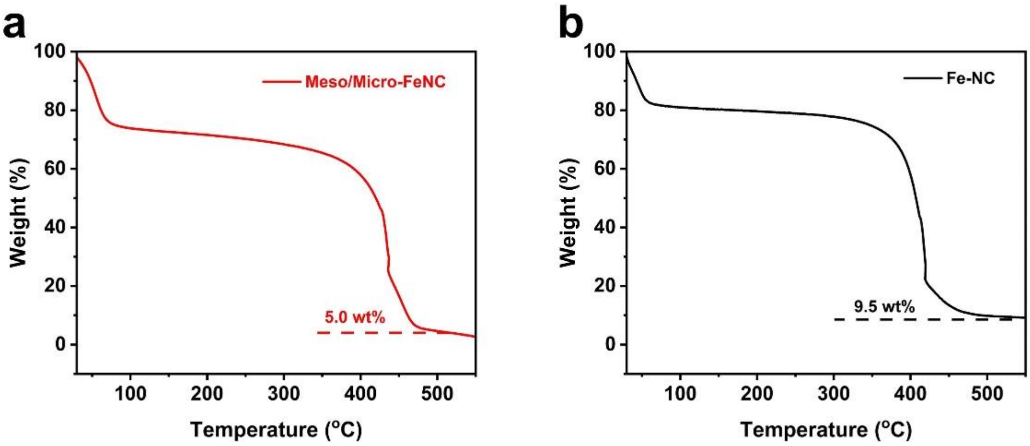

Figure S15. TGA curve of Meso/Micro-FeNC (a) and Fe-NC (b) in the atmosphere of flowing air.

Based on TG analysis conducted under air atmosphere with a heating rate of 10°C min^{-1} to 600°C, the residual mass fractions for Meso/Micro-FeNC and Fe-NC were measured as 5 wt% and 9.5 wt%, respectively. Assuming that the final residue is Fe_2O_3, the metal Fe content is calculated to be ≈ 3.50 wt% for Meso/Micro-FeNC and ≈ 6.64 wt% for Fe-NC.

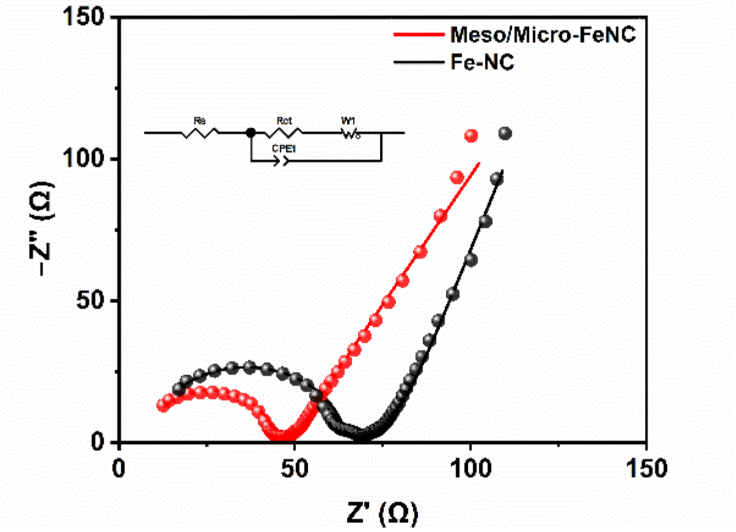

Figure S16. Nyquist and corresponding fitting plots of Meso/Micro-FeNC and Fe-NC, along with the corresponding equivalent circuit models.

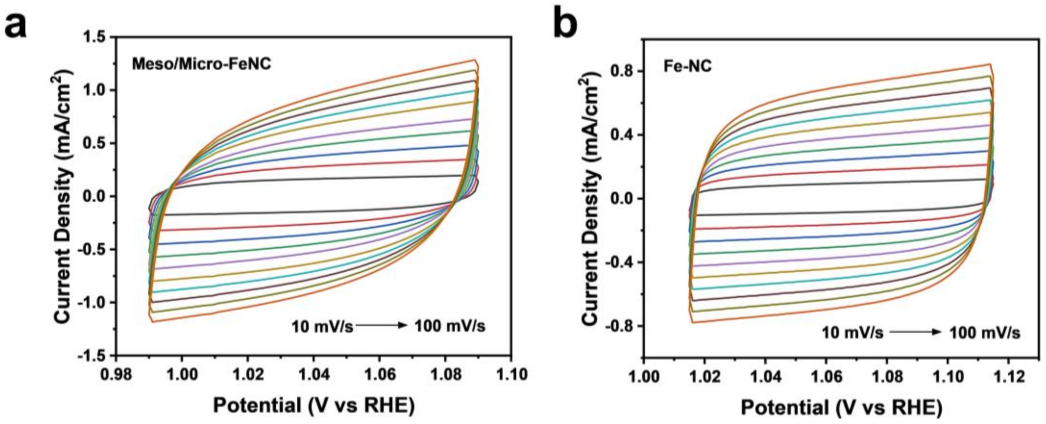

Figure S17. CV curves at different scan rates of Meso/Micro-FeNC (a) and Fe-NC (b).

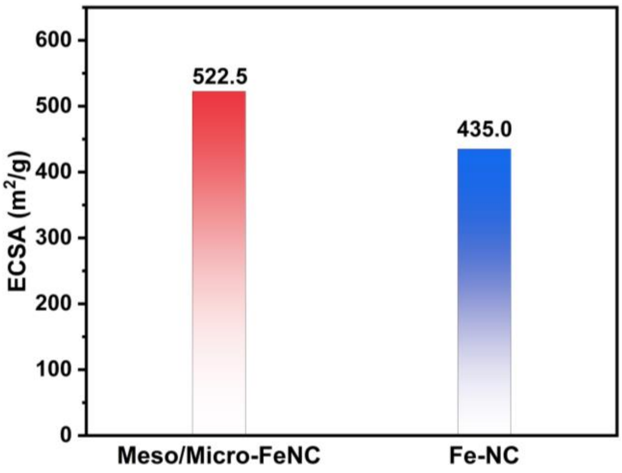

Figure S18. ECSA of Meso/Micro-FeNC and Fe-NC.

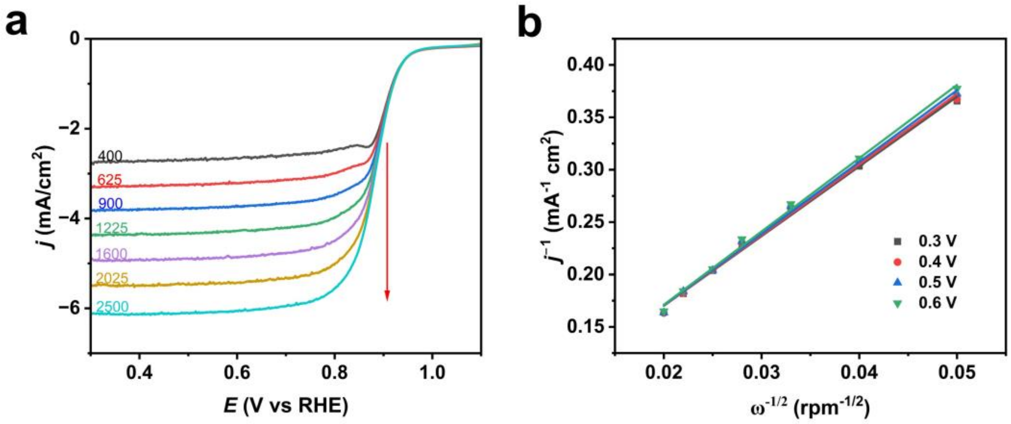

Figure S19. Polarization curves of Meso/Micro-FeNC at different rotating speeds (a). K-L plots for Meso/Micro-FeNC catalysts at varying potentials including the calculated electron transfer number (b).

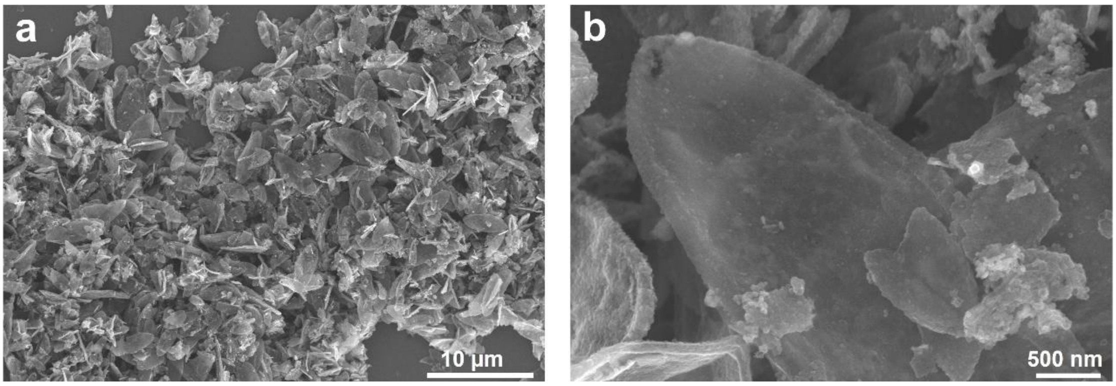

Figure S20. SEM images of Meso/Micro-FeNC after stability test.

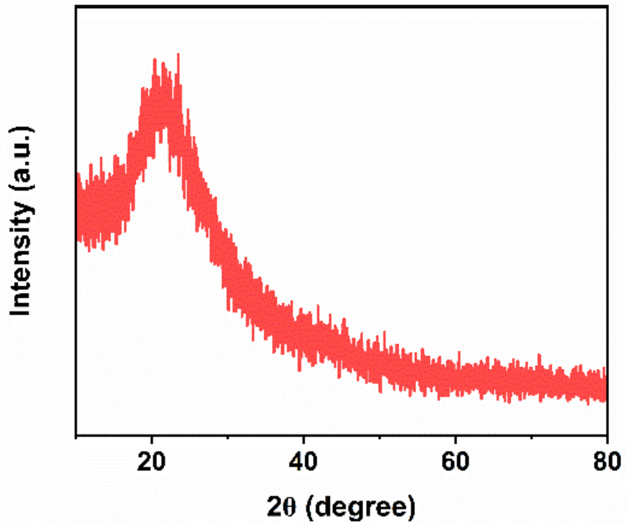

Figure S21. Powder XRD pattern of Meso/Micro-FeNC after stability test.

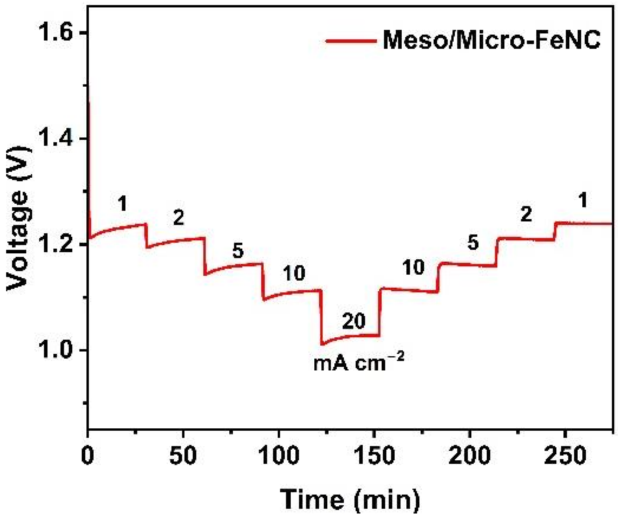

Figure S22. Galvanostatic discharge curves of Meso/Micro-FeNC-based ZAB at different current densities after long-term charge and discharge.

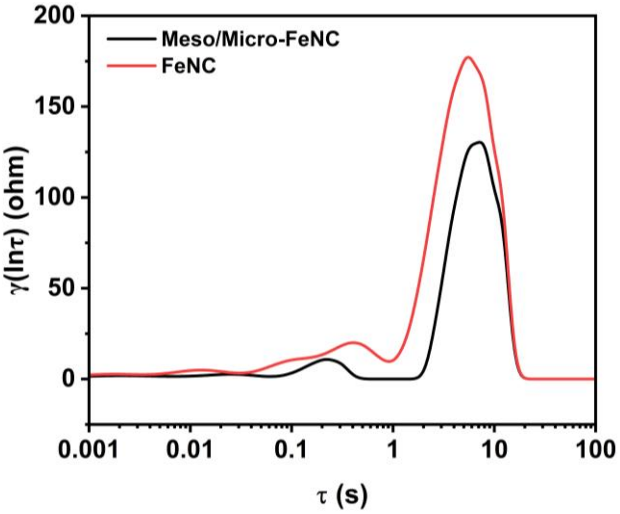

Figure S23. DRT analysis of Meso/Micro-FeNC and Fe-NC at Open circuit voltage (OCV).

Table S1 Mesoporous volume, Microporous volume, and Mesoporous/Microporous volume ratio of Meso/Micro-FeNC and Fe-NC

	Mesoporous volume (cm^3/g)	Microporous volume (cm^3/g)	Mesoporous/Microporous volume ratio
Meso/Micro-FeNC	0.22	0.26	0.84
Fe-NC	0.17	0.28	0.60

Table S2 Fitted kinetic parameters from EIS equivalent circuit for Meso/Micro-FeNC and Fe-NC

	Rct	W1-R	CPE1-T
Meso/Micro-FeNC	34.91	16.57	$8.96 \cdot 10^{-9}$
Fe-NC	55.45	43.95	$1.33 \cdot 10^{-8}$

Table S3. Comparison of the ORR and ZAB performance of Meso/Micro-FeNC and other similar materials

Catalysts	E_{onset}(mV)	$E_{1/2}$(mV)	Power density (mW/cm^2)	Specific capacity (mAh/g$_{Zn}$)	Ref.
	ORR		ZAB		
Fe/N-MGN	970	860	–	–	[9]
$F_{0.4}$NC	1064	872	–	–	[10]
Fe-NPC	990	880	–	–	[11]
Fe SA-NSC-900	940	860	–	–	[12]
$Fe_8Co_{0.2}$-NC-800	–	820	704 (3.5 mA/cm^2)	124.9	[13]
Zn/Fe-NC	1081	875	814.6 (10 mA/cm^2)	186.2	[14]
Fe_3Co-NC@900	1070	880	746.4 (5 mA/cm^2)	62.8	[15]
ZnCoFe-N-C	950	878	794.7 (50 mA/cm^2)	350	[16]
Co/CoFe@NC	970	840	775.2 (10 mA/cm^2)	146.6	[17]
ERG@Glu&Fe-40-Mel	981	861	766.3 (10 mA/cm^2)	132	[18]
SAC-FeN-WPC	990	850	735.6 (10 mA/cm^2)	152	[19]
Meso/Micro-FeNC	**990**	**880**	**787.63 (20 mA/cm^2)**	**146.7**	**This work**

REFERENCES

1. Wan, T. H.; Saccoccio, M.; Chen, C.; Ciucci, F. Influence of the discretization methods on the distribution of relaxation times deconvolution: implementing radial basis functions with DRTtools. *Electrochim. Acta* **2015**, *184*, 483-499. https://doi.org/10.1016/j.electacta.2015.09.097
2. Blöchl, P. E. Projector augmented-wave method. *Phys. Rev. B* **1994**, *50*, 17953-17979. https://doi.org/10.1103/PhysRevB.50.17953
3. Kresse, G.; Furthmüller, J. Efficiency of ab-initio total energy calculations for metals and semiconductors using a plane-wave basis set. *Comput. Mater. Sci* **1996**, *6*, 15-50. https://doi.org/10.1016/0927-0256(96)00008-0
4. Kresse, G.; Joubert, D. From ultrasoft pseudopotentials to the projector augmented-wave method. *Phys. Rev. B* **1999**, *59*, 1758-1775. https://doi.org/10.1103/PhysRevB.59.1758
5. Perdew, J. P.; Burke, K.; Ernzerhof, M. Generalized gradient approximation made simple. *Phys. Rev. Lett.* **1996**, *77*, 3865-3868. https://doi.org/10.1103/PhysRevLett.77.3865
6. Monkhorst, H. J.; Pack, J. D. Special points for brillouin-zone integrations. *Phys. Rev. B* **1976**, *13*, 5188-5192. https://doi.org/10.1103/PhysRevB.13.5188
7. Mathew, K.; Kolluru, V. S. C.; Mula, S.; Steinmann, S. N.; Hennig, R. G. Implicit self-consistent electrolyte model in plane-wave density-functional theory. *J. Chem. Phys.* **2019**, *151*, 234101. https://doi.org/10.1063/1.5132354
8. Nørskov, J. K.; Rossmeisl, J.; Logadottir, A.; et al. Origin of the overpotential for oxygen reduction at a fuel-cell cathode. *J. Phys. Chem. B* **2004**, *108*, 17886-17892. https://doi.org/10.1021/jp047349j
9. Xu, Y.; Zhu, L.; Cui, X.; et al. Graphitizing N-doped mesoporous carbon nanospheres via facile single atom iron growth for highly efficient oxygen reduction reaction. *Nano Res.* **2020,** *13*, 752-758. https://doi.org/10.1007/s12274-020-2689-9
10. Kim, D.; Nguyen, A. N.; Yoo, H. Iron doping of coordination polymer nanocubes and post-thermolysis for efficient oxygen reduction reaction single-atom catalysis. *J.*

Power Sources **2025,** *641*, 236812. https://doi.org/10.1016/j.jpowsour.2025.236812

11. Perumalsamy, M.; Yoon, Y.; Elumalai, V.; et al. Engineering spin state modulation through phosphorus-coordinated Fe-NC catalysts for enhanced ORR performance in flexible Al-air batteries. *Appl. Catal. B* **2025,** *372*, 125329. https://doi.org/10.1016/j.apcatb.2025.125329
12. Wang, M.; Yang, W.; Li, X.; et al. Atomically dispersed Fe-heteroatom (N, S) bridge sites anchored on carbon nanosheets for promoting oxygen reduction reaction. *ACS Energy Lett.* **2021,** *6*, 379-386. https://doi.org/10.1021/acsenergylett.0c02484
13. Jin, T.; Nie, J.; Dong, M.; et al. 3D interconnected honeycomb-like multifunctional catalyst for Zn-air batteries. *Nano-Micro Lett.* **2022,** *15*, 26. https://doi.org/10.1007/s40820-022-00959-6
14. Fu, C.; Qi, X.; Zhao, L.; et al. Synergistic cooperation between atomically dispersed Zn and Fe on porous nitrogen-doped carbon for boosting oxygen reduction reaction. *Appl. Catal. B* **2023,** *335*, 122875. https://doi.org/10.1016/j.apcatb.2023.122875
15. Srinivas, K.; Yu, H.; Chen, Z.; et al. Densely accessible Fe/Co-N_x dual-atom site coupled core-shell Co_3Fe_7@C as an efficient bifunctional oxygen electrocatalyst for rechargeable zinc-air batteries. *J. Mater. Chem. A* **2024,** *12*, 16863-16876. https://doi.org/10.1039/D4TA02444C
16. Li, G.; Deng, W.; He, L.; et al. Zn, Co, and Fe tridoped N-C core-shell nanocages as the high-efficiency oxygen reduction reaction electrocatalyst in zinc-air batteries. *ACS Appl. Mater. Interfaces* **2021,** *13*, 28324-28333. https://doi.org/10.1021/acsami.1c06750
17. Niu, Y.; Teng, X.; Gong, S.; et al. Engineering two-phase bifunctional oxygen electrocatalysts with tunable and synergetic components for flexible Zn-air batteries. *Nano-Micro Lett.* **2021,** *13*, 126. https://doi.org/10.1007/s40820-021-00650-2
18. Meng, J.; Zhang, Y.; Yin, X.; et al. A hydrophobic cathode design towards high-stability Zn-air batteries: Coupling FeTAP molecules with self-supporting edge-rich graphene membrane. *Chem. Eng. J.* **2025,** *515*, 163833. https://doi.org/10.1016/j.cej.2025.163833

19. Zhong, L.; Jiang, C.; Zheng, M.; et al. Wood carbon based single-atom catalyst for rechargeable Zn-air batteries. *ACS Energy Lett.* **2021,** *6*, 3624-3633. https://doi.org/10.1021/acsenergylett.1c01678